CONDENSED MATTER PHYSICS

Chemical identification through two-dimensional electron energy-loss spectroscopy

Renwen Yu[1] and F. Javier García de Abajo[1,2]*

We explore a disruptive approach to nanoscale sensing by performing electron energy loss spectroscopy through the use of low-energy ballistic electrons that propagate on a two-dimensional semiconductor. In analogy to free-space electron microscopy, we show that the presence of analyte molecules in the vicinity of the semiconductor produces substantial energy losses in the electrons, which can be resolved by energy-selective electron injection and detection through actively controlled potential gates. The infrared excitation spectra of the molecules are thereby gathered in this electronic device, enabling the identification of chemical species with high sensitivity. Our realistic theoretical calculations demonstrate the superiority of this technique for molecular sensing, capable of performing spectral identification at the zeptomol level within a microscopic all-electrical device.

INTRODUCTION

The spectral determination of vibrational and electronic excitations in molecules provides the means to detect and chemically identify small amounts of analyte (*1*), opening exciting applications in areas such as medical diagnosis (*2*, *3*) and detection of hazardous substances (*4*). In particular, all-optical techniques based on Raman and infrared (IR) absorption spectroscopies are widely used for this purpose (*5*, *6*) and can reach single-molecule sensitivity (*7*, *8*) when enhanced by the near-field light amplification of optical hot spots associated with plasmons—conduction electron excitations—localized at corrugated metal surfaces (*9*). Noninvasive far-field optical approaches are however limited in spatial resolution by diffraction (*10*), while near-field optics can resolve areas of a few tens of nanometers (*11*).

Atomic-scale spectral imaging is made possible by resorting to electron beams in electron microscopes, where localized optical excitations are revealed by analyzing the energy losses experienced by the electrons upon interaction with the sample. Recent advances in electron energy-loss spectroscopy (EELS) have pushed the combined space/energy resolution to unprecedented levels in the few milliectronvolts per subangstrom range (*12*–*14*), enabling the detection and spatial imaging of nanoscale optical excitations such as plasmons (*15*–*18*) and phonon polaritons (*12*–*14*). However, the use of swift electrons requires high vacuum and produces structural damage, which hinders applications to in vivo samples. In addition, damage also limits the acquisition of visible and IR spectra from structures consisting of only a few molecules (*19*, *20*). Aloof electron excitation can prevent this problem by probing excitations in a material without physically traversing it (*21*), an approach that has been used to map optical modes in metallic nanoparticles (*17*), including those confined to narrow gaps (*22*), but has not yet been applied to resolve localized IR molecular fingerprints for chemical analysis.

The spatial range of interaction between an electron moving with velocity v and an excitation of frequency ω is dictated by v/ω (*23*). For small electron-sample separations R compared with this distance, the interaction strength is dominated by the radial component of the electric field carried by the electron, the intensity of which scales as $1/(vR)^2$. Besides the advantage of reduced damage, low electron energies favor the interaction strength, as it is well known in the context of low-energy electron microscopy (*24*). However, an integrable approach without the need of vacuum technology would be desirable to perform spectral optical analysis as an alternative to the existing bulky electron microscope setups. Ballistic electrons moving in two-dimensional (2D) materials such as graphene (*25*–*27*) and monolayer transition metal dichalcogenides (TMDs) (*28*–*36*) could be used for this purpose, as they already feature vertical layer confinement without the need of a vacuum chamber, and their energies lie in the subelectronvolt regime, thus anticipating large inelastic interaction with neighboring molecules. In a parallel effort, transport and steering of ballistic electrons have been recently explored in graphene (*37*–*40*) and other 2D systems (*41*) as a platform for 2D electron microscopy. In addition, gas sensors have been realized using graphene by exploiting the variation in electrical resistivity induced by charge transfer from the molecules (*42*, *43*). However, these schemes lack the spectral resolution needed to identify molecular fingerprints for chemical analysis.

Here, we propose a disruptive approach toward chemical identification of zeptomol amounts of analyte through an all-electrical device capable of quantitatively resolving the spectral fingerprints of the sampled molecules. We rely on ballistic electrons moving within a 2D semiconductor, in which they are injected with well-defined energy through an engineered gate. Inelastic losses produced by the molecules are then resolved as features in the current transmitted after the electrons are energy filtered by an additional tunable exit gate. Our realistic simulations reveal a sensitivity down to the zeptomol level within a device of ~1 μm^2 footprint, which could be integrated for massive multiplexing using currently available technology.

RESULTS AND DISCUSSION

We present a sketch of our proposed device in Fig. 1A. Ballistic electrons are injected by an emitter into the conduction band of a 2D semiconductor with well-defined energy E_i. The interaction of these electrons with analyte molecules placed in the vicinity of the semiconductor produces energy losses $\hbar\omega$ associated with the excitation fingerprints of those molecules. The electron-molecule

[1]ICFO-Institut de Ciències Fòtoniques, Barcelona Institute of Science and Technology, 08860 Castelldefels (Barcelona), Spain. [2]ICREA-Institució Catalana de Recerca i Estudis Avançats, Passeig Lluís Companys 23, 08010 Barcelona, Spain.
*Corresponding author. Email: javier.garciadeabajo@nanophotonics.es

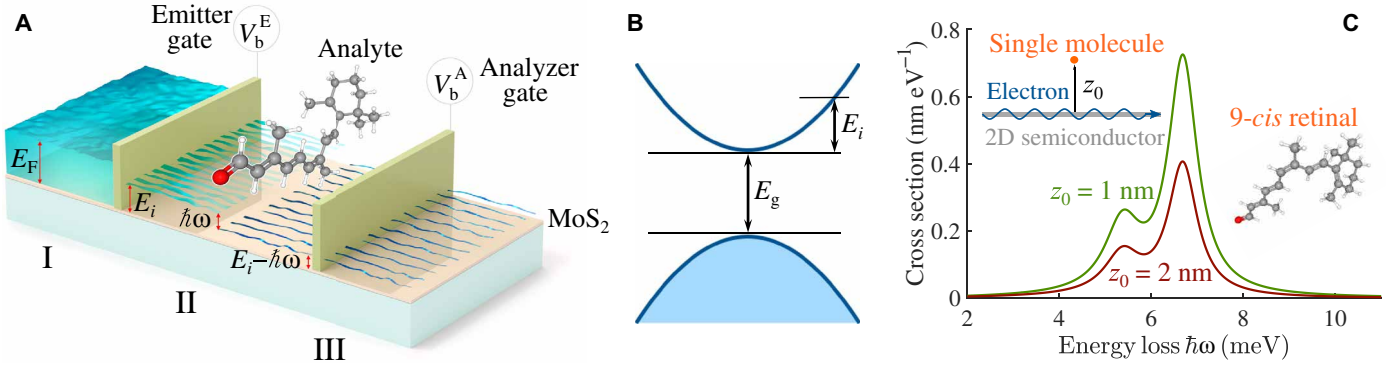

Fig. 1. Two-dimensional electron energy-loss spectroscopy (2D-EELS). (**A**) Sketch of the proposed device. An electron emitter (tunable through a voltage V_b^E) injects ballistic electrons of well-defined energy E_i into the conduction band of a 2D semiconductor (MoS_2). These electrons interact inelastically with a neighboring molecule (analyte) placed outside the material, producing characteristic excitations (energy $\hbar\omega$) at the expense of the electron energy. Detection and spectral analysis of the transmitted electrons (through an analyzer tunable through a voltage V_b^A) reveal the chemical identity of the analyte by resolving its excitation fingerprints. (**B**) Schematic band structure of a MoS_2 monolayer semiconductor (effective mass $m^* = 0.55\ m_e$, gap energy $E_g = 1.58$ eV) with E_i referred to the CBB and satisfying $E_i < E_g$ to prevent electron decay by coupling to interband transitions. (**C**) Spectral cross section for the inelastic interaction between an electron plane wave of energy $E_i = 12$ meV moving in monolayer MoS_2 and a single 9-*cis* retinal molecule for two molecule-semiconductor distances z_0.

inelastic interaction strength is then spectrally resolved by recording energy-filtered electrons through a narrow-band transmission gate (electron detector) as a function of their final energy $E_i - \hbar\omega$. EELS spectra are acquired by sweeping ω, therefore providing spectral identification of the molecules. TMD monolayers are good candidates to be used as the 2D semiconductor for the present application, as they feature direct bandgaps of ~2 eV (*29*–*33*), which can be tuned by several methods (*34*–*36*). Specifically, we consider monolayer MoS_2, which features a direct gap energy $E_g = 1.58$ eV and a nearly parabolic conduction band with effective mass $m^* = 0.55\ m_e$ (*44*). We consider the semiconductor to lie on top of a substrate of permittivity $\epsilon_s = 4$, which provides the electrical isolation needed to define gate potential profiles (see below), for example, through laterally patterned back gates. We further restrict the injected electron energy relative to the conduction band bottom (CBB) to satisfy the condition $E_i < E_g$, which guarantees that electron-electron scattering associated with interband transitions is energetically forbidden (Fig. 1B), thus resulting in longer phonon-limited mean free paths.

The theory needed to calculate EELS probabilities is well established in the context of transmission electron microscopy and generally leads to excellent agreement with experiment by simply describing the electron-sample interaction within first-order pertubation (*23*). Here, we adapt such EELS formalism to deal with the particular situation of 2D ballistic electrons and calculate the tunneling current using a well-established procedure based on the Landauer formalism (*45*). In this context, inelastic electron-molecule interactions play a similar role in our EELS derivation (see details in Methods) as electron-phonon scattering during electron transport in 2D materials (*46*), and the current approach is valid for high-quality samples characterized by large ballistic mean free paths. Specifically, we describe the molecules in terms of their polarizabilities. For concreteness, we consider 9-*cis* retinal (*47*), which features a strong optical response in the far-IR spectral region, where the device is intended to operate for chemical identification. The calculated inelastic scattering cross section of a single molecule (averaged over molecular orientations) is spectrally resolved in Fig. 1C for $E_i = 12$ meV electrons and molecule-surface separations $z_0 = 1$ and 2 nm. The cross section takes substantial values of a fraction of the molecular lateral size when integrated over the strong ~6.77 meV absorption features. As anticipated above, the cross section increases with decreasing electron energy (roughly as $1/v^2 \sim 1/E_i$) down to the threshold $E_i = \hbar\omega$ (see fig. S1), an effect that could be exploited to maximize the inelastic signal when targeting specific molecular fingerprints.

A design of an electron emitter gate is shown in Fig. 2A, consisting of a potential barrier that hosts a central well. Tunneling through the barrier can be resonantly assisted by coupling to trapped quantum well states (QWSs) (*48*), leading to full transmission maxima (Fig. 2B). In a related context, gates of larger size have been experimentally explored with lower-energy electrons in semiconductors (*49*, *50*). The more deeply bound the trapped state, the weaker its leakage to the surrounding regions and, consequently, the sharper the transmission resonance. The present gate hosts a single QWS of energy $E^w \sim 12$ meV. We further avoid coupling to higher-energy resonances (the ~14-meV feature) by placing the Fermi energy of the region to the left of the gate slightly above E^w (see below). The energy of transmitted electrons can be directly raised by increasing the well voltage V_b^E, with higher energies resulting in broader transmitted spectra, in accordance with the mentioned increase in width produced by leakage out from the QWS when its energy gets closer to the barrier height (Fig. 2C).

Similarly, the analyzer gate must feature monochromatic transmission over a wide energy range. In addition, it is desirable that it blocks unscattered electrons to enhance the relative inelastic signal in the electron transmission through the device. A tunable analyzer potential configuration that satisfies both of these conditions is presented in fig. S2.

Coming back to the sketch of our 2D EELS device illustrated in Fig. 1A, it incorporates emitter and analyzer gates, the transmission of which can be tuned by varying their well voltages V_b^E and V_b^A, respectively. Electrons are injected with energy E_i from region I (where the Fermi energy E_F is moved into the conduction band at an energy slightly above the first QWS of the analyzer) into region II (width L, where the molecules are deposited). We consider a molecular density $n_{mol} = 10^3\ \mu m^{-2}$ and a 2-nm separation between molecules and the monolayer MoS_2 semiconductor. This short separation could be realized, for instance, by passivating the latter

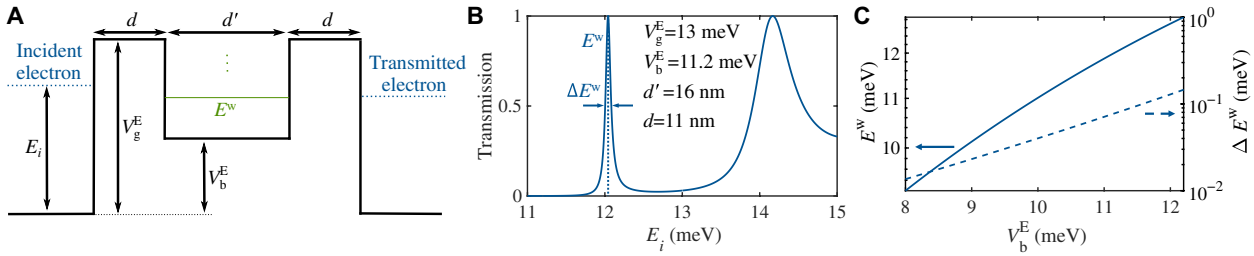

Fig. 2. Electron emission gate. (**A**) Schematic 1D potential configuration for quasi-monochromatic electron injection. The potential energy (vertical direction) defines the position-dependent CBB. Tunneling through the double potential barrier is assisted by resonant coupling to an intermediate quantum well state. (**B**) Electron transmission as a function of electron energy for gate parameters d = 11 nm, d' = 16 nm, V_g^E = 13 meV, and V_b^E = 11.2 meV. (**C**) Energy and full width at half maximum of the first transmission peak as a function of bias voltage V_b^E for fixed V_g^E = 13 meV.

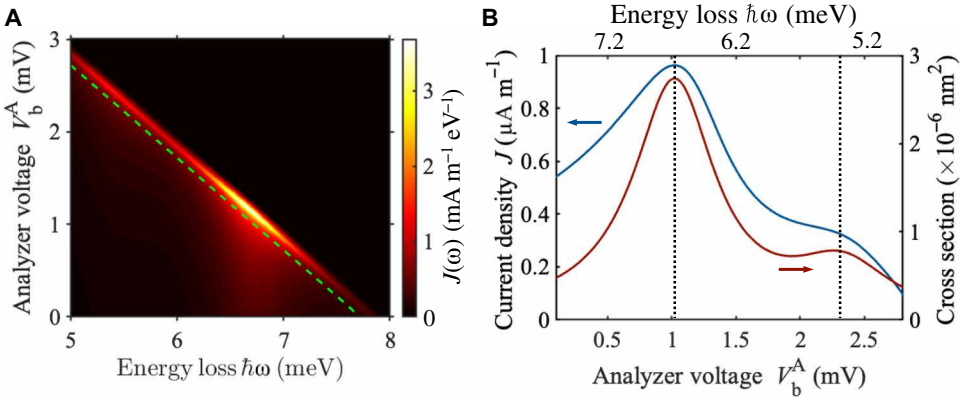

Fig. 3. EELS probability in a 2D electron microscope. We consider the device depicted in Fig. 1A with region I doped to a Fermi energy E_F = 12.1 meV, the emitter gate of Fig. 2B, and the analyzer gate (see details in fig. S2) filtering the transmission of inelastically scattered electrons (energy $E_i - \hbar\omega$) from II to III by varying the voltage V_b^A. (**A**) Spectral current density $J(\omega)$ of electrons transmitted through the entire device, plotted as a function of electron energy loss and analyzer gate voltage V_b^A. We assume a molecular layer density $n_{mol} = 10^3\ \mu m^{-2}$ in region II, spanning a width L = 1 μm and a molecule MoS_2 distance z_0 = 2 nm. (**B**) Total ω-integrated transmitted current density J as a function of analyzer voltage V_b^A, compared with the IR optical absorption spectrum of 9-*cis* retinal. The upper and lower horizontal axes are related through $\hbar\omega = 7.72\ \text{meV} - e\,V_b^A$, which corresponds to the dashed line in (A). Vertical dotted lines mark the two dominant resonances of the molecule.

with a six-monolayer boron nitride film, as done in state-of-the-art experiments (*51*). We note that the overlap between the out-of-plane component of the electron wave function and the molecule is significantly reduced for separation distances $z_0 \geq 1$ nm (*52*). After inelastic scattering by the molecules, electrons are finally transmitted with tunable energy $E_i - \hbar\omega$, thus revealing the molecular excitation spectrum as a function of excitation frequency ω.

The gate potentials are assumed to have translational invariance along the surface direction perpendicular to the plane of Fig. 2A, so we eventually quantify the transmitted electron current normalized per unit of length along that direction. We compute the resulting current density $J(\omega) \propto n_{mol} \times L$ from the product of transmission factors associated with the two gates and the frequency-resolved molecule inelastic cross section, after integrating over all possible electron energies $E_i < E_F$ (see region I in Fig. 1A) and in-plane directions (see Eq. 8 in Methods). The result is plotted in Fig. 3A as a function of energy loss $\hbar\omega$ and analyzer well voltage V_b^A for a width L = 1 μm of region II. Two bright features are observed, corresponding to the two inelastic scattering peaks of 9-*cis* retinal in the selected energy loss range (cf. Figs. 1C and 3A). We find an almost linear correlation between the peak energy loss contribution and the gate voltage $\hbar\omega = 7.72\ \text{meV} - e\,V_b^A$ [Fig. 3A, green dashed line, which is slightly redshifted with respect to the spectral maximum of $J(\omega)$ due to the strong spectral asymmetry of this function]. This enables us to retrieve spectra by measuring the ω-integrated transmitted current as a function of V_b^A. Actually, the device can only provide information as a function of the applied gate voltages, so the measured signal corresponds to the ω-integrated current.

The total current $J = \int d\omega\, J(\omega)$ is plotted in Fig. 3B (blue curve, left vertical axis) as a function of analyzer gate voltage V_b^A (lower horizontal axis). We take E_F = 12.1 meV in region I slightly above the E_i = 12 meV transmission peak so that electrons injected by the emitter gate (120 nA/μm current) are mainly directed along the in-plane normal to the gate. In addition, inelastic scattering by the molecule is mainly focused along the forward direction (see fig. S3), thus introducing only a minor contribution to spectral broadening of the signal transmitted through the analyzer gate (i.e., for a selected transmitted energy along the in-plane gate-normal direction). For comparison, we provide the dominant energy loss $\hbar\omega$ according to the above linear relation in the upper horizontal axis. The EELS spectrum thus generated bears a close correlation with the optical absorption spectrum of 9-*cis* retinal molecules (Fig. 3B, red curve, right vertical axis). This corroborates the spectral resolution of our proposed device, which, in particular, is sufficient to distinguish between different molecules,

such as 9-*cis* and all-cis retinal (see fig. S4). Incidentally, the inelastic current is reasonably large, translating into measurable values of 0.6 pA per zeptomol at the peak of Fig. 3B. Incidentally, the traveling time for a width $L = 1$ μm of the sampling region II is $L/\sqrt{2\,m^* E_i} \sim 20$ ps, compatible with pulsed injection for lock-in detection using currently available technology.

CONCLUSIONS

In summary, on the basis of realistic theoretical simulations, we have demonstrated the viability of a disruptive approach toward chemical detection and identification, in which molecular fingerprints associated with far-IR optical excitations are resolved as spectral features in the current transmitted through our proposed device as a function of applied gate voltages. This strategy circumvents the long-standing terahertz gap problem by resorting to electrons rather than photons as probes of molecular spectra. In this study, we have engineered emitter and analyzer gates to provide a direct reading of the molecular spectrum through the voltage-dependent profile of the current transmitted through the device. Nevertheless, simpler gate designs (e.g., single barrier potentials) could yield similar information by inspecting the derivatives of the transmitted current with respect to the emitter and analyzer barrier voltages. For simplicity, we have ignored multiple scattering by the potential barriers, which, in the absence of intrinsic inelastic attenuation, is an unavoidable effect. In practice, the intrinsic inelastic mean free path is finite, so we could adjust the size of the sampling region (II in Fig. 1A) to such length scale, thus avoiding multiple reflections while optimizing the signal due to the molecules. In addition, an out-of-plane magnetic field could be used to selectively steer the electrons, as already demonstrated in experiment (*37*–*41*); actually, this approach provides an alternative way of resolving the transmitted electron energy if an array of exit gates is used to detect different energy-dependent deflections or just using a single gate and scanning the strength of the magnetic field. Magnetic fields and lateral bias could also be used in combination with the lock-in injection noted above to drain electrons that are not scattered by the molecules without altering the in-plane normal energy that conveys the targeted spectral information. We note that a conducting tip could be used as an alternative electron source instead of electrical gates, as routinely done in the context of scanning tunneling microscopy, where elastic electrons are injected with atomic spatial resolution, thus suggesting a promising approach to improve imaging capabilities in the concept that we are exploring. A critical aspect of the present device is the ability of the 2D material to propagate hot electrons without inelastic losses over sufficiently long distances between the emitter and analyzer gates. The required electron energy has to exceed the sampled molecular modes, lying in the far-IR for the 9-*cis* retinal molecule here considered. For other macromolecules, where resonances can be localized at specific functional groups (e.g., vibrations in specific bonds in proteins), our formalism could be adapted by associating an effective polarizability with those groups rather than the entire molecule. As an alternative to 2D semiconductors, high-quality graphene is predicted to display mean free paths reaching hundreds of nanometers for the electron energies that we target here, according to detailed many-body theory (*53*). In addition, instead of monolayer MoS_2, thin MoS_2 multilayers should be explored because of their higher mobility, although stronger screening is also expected. Indirect bandgap materials could equally be advantageous to avoid interband transitions and minimize electron-electron scattering. Yet another alternative consists in exploiting ballistic transport in carbon nanotubes, in which light emission has been observed by electron-hole recombination after propagation over long mean free paths (*54*). We remark that the proposed chemical identification approach relies on planar solid-state devices, which due to their small footprints ~1 μm^2 could be integrated in a millimeter setup comprising millions of sampling elements for massive multiplexing. Spectral microscopy could thereby be performed with a spatial resolution limited by the footprint.

METHODS

Screened interaction

We consider a system formed by a 2D material (blue), lying at the interface between two homogeneous media ($z = 0$ plane) of permittivities ϵ_1 and ϵ_2, in the presence of a neighboring molecule (red) placed at position r_0 in medium 1, as depicted in Fig. 4A. We work in the quasi-static limit because the size and surface separation of the molecule are small compared with the light wavelength associated with its excitation fingerprints. The response of the system is then captured by the screened interaction $W(\mathbf{r}, \mathbf{r}', \omega)$, which is defined as the electric potential produced at a position $\mathbf{r}$ by a point charge placed at $\mathbf{r}'$ and oscillating over time with frequency ω as $e^{-i\omega t}$. We treat the 2D material as an infinitesimally thin layer of wave vector– and frequency-dependent surface conductivity $\sigma(k_\parallel, \omega)$, while the molecule is described as a point particle of 3×3 polarizability tensor $\alpha(\omega)$. In the absence of molecule and interface, the Coulomb interaction in medium 1 reduces to

$$W^1(\mathbf{r}-\mathbf{r}') = \frac{1}{\epsilon_1}\frac{1}{|\mathbf{r}-\mathbf{r}'|} = \frac{1}{\epsilon_1}\int \frac{d^2\mathbf{k}_\parallel}{2\pi k_\parallel} e^{i\mathbf{k}_\parallel \cdot (\mathbf{R}-\mathbf{R}') - k_\parallel |z-z'|} \quad (1)$$

where we use the notation $\mathbf{r} = (\mathbf{R}, z)$, with $\mathbf{R} = (x, y)$. The molecule and interface add contributions to $W = W^1 + W^{ref} + W^{mol}$ arising from surface reflection (W^{ref}, blue) and scattering by the molecule (W^{mol}, red), as illustrated in Fig. 4B. A self-consistent dipole p is induced at the molecule (green), which must incorporate its image self-interaction (thin green arrows).

Reflection at the interface

In the quasi-static limit, the reflection at the planar interface is fully captured by the Fresnel coefficient for p polarization $r_p = (\epsilon_2 - \epsilon_1 + 4\pi i\sigma k_\parallel/\omega)/(\epsilon_2 + \epsilon_1 + 4\pi i\sigma k_\parallel/\omega)$, which bears a nonlocal dependence

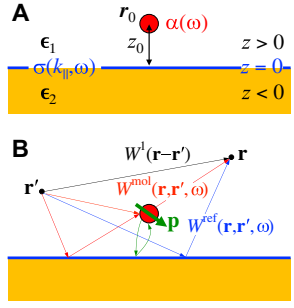

Fig. 4. Elements involved in the dielectric response of the system under consideration. (**A**) Optical response functions. (**B**) Decomposition of the screened interaction.

on $k_\parallel$ inherited from $\sigma(k_\parallel, \omega)$. In the present analysis, we approximate the response of MoS_2 by taking (*55*) $\sigma = (i\omega/4\pi)(1-\epsilon)d$ with a far-IR in-plane permittivity (*56*) $\epsilon \sim 16$ and layer thickness (*57*) $d = 0.65$ nm, while we take $\epsilon_1 = 1$ and $\epsilon_2 = 4$ to represent a substrate of moderate permittivity. We note that electron motion in the semiconductor is driven by in-plane electric fields, which are continuous across the interface, thus removing any ambiguity regarding the location of induced charges in either medium 1 or 2. Following previously described methods (*58*), we consider a p-polarized plane wave $e^{i\mathbf{k}_\parallel \cdot \mathbf{R} - ik_z z}$ $(-\mathbf{k}_\parallel k_z - k_\parallel^2 \hat{\mathbf{z}})$ incident from $z > 0$ (medium 1) and its reflection $r_p e^{i\mathbf{k}_\parallel \cdot \mathbf{R} + ik_z z}$ $(\mathbf{k}_\parallel k_z - k_\parallel^2 \hat{\mathbf{z}})$, where $k_z = \sqrt{k^2 \epsilon_1 - k_\parallel^2}$ and $k = \omega/c$; in the quasi-static limit ($c \to \infty$), we have $k_z \to ik_\parallel$, so the normal electric field reduces to $-k_\parallel^2 e^{i\mathbf{k}_\parallel \cdot \mathbf{R}}(e^{k_\parallel z} + r_p e^{-k_\parallel z})$, which corresponds to an electric potential $k_\parallel e^{i\mathbf{k}_\parallel \cdot \mathbf{R}}(e^{k_\parallel z} - r_p e^{-k_\parallel z})$; we then conclude that each component of externally incident potential $e^{i\mathbf{k}_\parallel \cdot \mathbf{R} + k_\parallel z}$ generates a reflected potential $-r_p e^{i\mathbf{k}_\parallel \cdot \mathbf{R} - k_\parallel z}$. For a source at $\mathbf{r}'$, this prescription allows us to directly write from Eq. 1 the reflection component of the screened interaction

$$W^{\mathrm{ref}}(\mathbf{r}, \mathbf{r}', \omega) = -\frac{1}{\epsilon_1} \int \frac{d^2 \mathbf{k}_\parallel}{2\pi k_\parallel} e^{i\mathbf{k}_\parallel \cdot (\mathbf{R} - \mathbf{R}') - k_\parallel (z + z')} r_p \tag{2}$$

which is valid for $z, z' \geq 0$ in medium 1.

Scattering by the molecule

A dipole $\mathbf{p}$ is induced at the molecule (position $\mathbf{r}_0$) by the test charge at $\mathbf{r}'$, giving rise to an induced potential $W^{\mathrm{mol}}(\mathbf{r}, \mathbf{r}', \omega) = \mathbf{p} \cdot \nabla_{\mathbf{r}_0}[W^1(\mathbf{r} - \mathbf{r}_0) + W^{\mathrm{ref}}(\mathbf{r}, \mathbf{r}_0, \omega)]$. Using Eqs. 1 and 2, we find

$$\begin{aligned} W^{\mathrm{mol}}(\mathbf{r}, \mathbf{r}'\omega) = \frac{1}{\epsilon_1} \int \frac{d^2 \mathbf{k}_\parallel}{2\pi k_\parallel} e^{i\mathbf{k}_\parallel \cdot (\mathbf{R} - \mathbf{R}_0) - k_\parallel z_0} \\ \times (r_p e^{-k_\parallel z} - e^{k_\parallel z})(i\mathbf{k}_\parallel + k_\parallel \hat{\mathbf{z}}) \cdot \mathbf{p} \end{aligned} \tag{3}$$

for $0 \leq z < z_0$. The dependence on $\mathbf{r}'$ is carried by $\mathbf{p}$, which must satisfy the self-consistent relation

$$\alpha^{-1} \cdot \mathbf{p} = -\nabla_{\mathbf{r}_0}[W^1(\mathbf{r}_0 - \mathbf{r}') + W^{\mathrm{ref}}(\mathbf{r}_0, \mathbf{r}', \omega)] + \mathcal{G} \cdot \mathbf{p}$$

where the $\nabla_{\mathbf{r}_0}$ term represents the sum of direct and reflected potentials due to the charge at $\mathbf{r}'$, whereas the rightmost term accounts for the dipole image self-interaction through (*58*)

$$\begin{aligned} \mathcal{G}(\omega) &= -\nabla_{\mathbf{r}_1} \otimes \nabla_{\mathbf{r}_2} W^{\mathrm{ref}}(\mathbf{r}_1, \mathbf{r}_2, \omega) \mid_{\mathbf{r}_1 = \mathbf{r}_2 = \mathbf{r}_0} \\ &= \begin{pmatrix} G/2 & 0 & 0 \\ 0 & G/2 & 0 \\ 0 & 0 & G \end{pmatrix} \end{aligned}$$

with

$$G = \frac{1}{\epsilon_1} \int_0^\infty k_\parallel^2 \, \mathrm{d}k_\parallel \, r_p e^{-2k_\parallel z_0} \tag{4}$$

Solving for $\mathbf{p}$ and using Eqs. 1 and 2, we find

$$\begin{aligned} \mathbf{p} = \frac{1}{\epsilon_1} \frac{1}{(\alpha^{-1} - G)} \cdot \int \frac{d^2 \mathbf{k}_\parallel}{2\pi k_\parallel} e^{i\mathbf{k}_\parallel \cdot (\mathbf{R}_0 - \mathbf{R}') - k_\parallel z_0} \\ \times (r_p e^{-k_\parallel z'} - e^{k_\parallel z'})(i\mathbf{k}_\parallel - k_\parallel \hat{\mathbf{z}}) \end{aligned} \tag{5}$$

which together with Eq. 3 permits calculating W^{mol} for $0 \leq z, z' < z_0$.

2D electron energy-loss spectroscopy

Following a previous analysis in the context of transmission electron microscopy (*23*), we use the expression $\Gamma_{fi} = \int_0^\infty d\omega \, \Gamma_{fi}(\omega)$ with

$$\begin{aligned} \Gamma_{fi}(\omega) = 2e^2 \int d^3 \mathbf{r} \int d^3 \mathbf{r}' \, \psi_f(\mathbf{r}) \psi_i^*(\mathbf{r}) \psi_f^*(\mathbf{r}') \psi_i(\mathbf{r}') \\ \times \mathrm{Im}\{-W(\mathbf{r}, \mathbf{r}', \omega)\} \, \delta(E_f - E_i + \hbar\omega) \end{aligned} \tag{6}$$

to calculate the rate of transitions between initial and final electron states ψ_i and ψ_f of energies E_i and E_f, respectively. More precisely, $\Gamma_{fi}(\omega)$ is the loss rate associated with an energy transfer $\hbar\omega$ to the sample. We now apply this formalism to ballistic electrons moving in the 2D material by expressing their wave functions as $\psi_{i,f}(\mathbf{r}) = A^{-1/2} e^{i\mathbf{Q}_{i,f} \cdot \mathbf{R}} \psi^\perp(z)$, where A is the normalization area, $\mathbf{Q}_{i,f}$ are the 2D electron wave vectors, and $\psi^\perp(z)$ is the out-of-plane electron wave function, assumed to be state independent and subject to the normalization condition $\int dz \, |\psi^\perp(z)|^2 = 1$. Inserting these wave functions into Eq. 6, we find

$$\begin{aligned} \Gamma_{fi}(\omega) = \frac{2e^2}{A^2} \int d^2 \mathbf{R} \int d^2 \mathbf{R}' \, e^{-i\mathbf{k}_\parallel \cdot (\mathbf{R} - \mathbf{R}')} \\ \times \mathrm{Im}\{-W(\mathbf{R}, 0, \mathbf{R}', 0, \omega)\} \, \delta(E_f - E_i + \hbar\omega) \end{aligned} \tag{7}$$

where $\mathbf{k}_\parallel = \mathbf{Q}_i - \mathbf{Q}_f$ is the wave vector transfer, and we assume for simplicity that $\psi^\perp$ extends a negligible distance away from the 2D material plane $z = 0$ (i.e., we only need to evaluate W at $z = z' = 0$). In addition, $E_{i,f} = \hbar^2 Q_{i,f}^2 / 2m^*$, where m^* is the effective mass of the parabolic semiconductor conduction band. We further assume medium 1 to have real permittivity ϵ_1, so that W^1 is real and does not contribute to create inelastic transitions.

We now integrate Eq. 7 over final states by adopting the customary prescription $\sum_f \to (A/4\pi^2) \int d^2 \mathbf{Q}_f$. Then, using Eqs. 2, 3, and 5, we find

$$\Gamma_i = \sum_f \Gamma_{fi} = \Gamma_i^{\mathrm{ref}} + \Gamma_i^{\mathrm{mol}}$$

with

$$\begin{aligned} \Gamma_i^{\mathrm{ref}}(\omega) &= \frac{e^2 m^*}{\pi \epsilon_1 \hbar^2} \theta(E_i - \hbar\omega) \int \frac{d\varphi}{k_\parallel} \mathrm{Im}\{r_p\}, \\ \Gamma_i^{\mathrm{mol}}(\omega) &= \frac{2e^2 m^*}{\epsilon_1^2 \hbar^2 A} \theta(E_i - \hbar\omega) \int \frac{d\varphi}{k_\parallel^2} e^{-2k_\parallel z_0} \\ &\quad \times \mathrm{Im}\left\{(r_p - 1)^2 (\mathbf{k}_\parallel - i k_\parallel \hat{\mathbf{z}}) \cdot \frac{1}{\alpha^{-1} - \mathcal{G}} \cdot (\mathbf{k}_\parallel + i k_\parallel \hat{\mathbf{z}})\right\} \end{aligned}$$

where $k_\parallel = (Q_i^2 + Q_f^2 - 2Q_i Q_f \cos\varphi)^{1/2}$, $Q_f = (Q_i^2 - 2m^*\omega/\hbar)^{1/2}$, and φ is the scattering angle.

The rate Γ_i^{ref} originates in intrinsic inelastic processes of the 2D material and surrounding homogeneous media, whereas Γ_i^{mol} results from the interaction with the molecule. In this study, we assume lossless dielectrics (i.e., real $\epsilon_{1,2}$ and imaginary σ), leading to $\Gamma_i^{\mathrm{ref}} = 0$. This is consistent with the condition $E_i < E_g$ for ballistic propagation. A small inelastic scattering associated with phonons or disorder could be easily incorporated through a phenomenological intrinsic mean free path.

Electron scattering cross section

We find it convenient to extract an inelastic molecule cross section $\sigma_i^{\mathrm{mol}} = \Gamma_i^{\mathrm{mol}}/(v_i/A)$, where we divide by the electron flux v_i/A given in terms of the initial electron velocity $\mathbf{v}_i = \hbar\mathbf{Q}_i/m^*$. In the present study, we assume an isotropic polarizability (see below) and a lossless surface (real r_p), so the scattering angle– and transition frequency–resolved differential cross section reduces to (for $\hbar\omega < E_i$)

$$\sigma_i^{\mathrm{mol}}(\omega,\varphi) = \frac{2e^2 m^*}{\epsilon_1^2 \hbar^2 v_i} \mathrm{e}^{-2k_{\parallel} z_0} (r_p - 1)^2 \times \mathrm{Im}\left\{ \frac{1}{\alpha^{-1} - G/2} + \frac{1}{\alpha^{-1} - G} \right\}$$

with G defined by Eq. 4. Plots of $\sigma_i^{\mathrm{mol}}(\omega,\varphi)$ are provided in fig. S3. The angle-integrated spectrally resolved cross section is given by $\sigma_i^{\mathrm{mol}}(\omega) = \hbar^{-1}\int d\varphi\ \sigma_i^{\mathrm{mol}}(\omega,\varphi)$, which is plotted in Fig. 1C and has units of length (i.e., the effective length scattered by the molecule from the incident 2D electron plane wave) per unit energy.

Tunneling current density

We consider the device of Fig. 1A and choose the x and y in-plane directions to be oriented perpendicular and parallel to the potential barriers, respectively. The left-to-right inelastic current density (per unit of barrier length) that is transmitted through the device can be calculated as $J = -(2e/A)\sum_{\mathbf{Q}_i} v_{ix} T(\mathbf{Q}_i)$ (*59*), where the sum extends over electrons incident from region I with wave vector $\mathbf{Q}_i$, transversal velocity v_{ix}, and energy within the $0 \le E_i \le E_F$ range. The factor of 2 in this expression accounts for spin degeneracy, while A is a quantization area. Neglecting multiple scattering by molecules or potential barriers, the transmission coefficient can be written as the product $T(\mathbf{Q}_i) = T_E(Q_{ix})\ [L'\, n_{\mathrm{mol}} \int d\omega \int d\varphi\ \sigma_i^{\mathrm{mol}}(\omega,\varphi)]\ T_A(Q_{fx})$, where n_{mol} is the areal molecule density in region II, whereas the transmission coefficients of the emitter and analyzer barriers T_E and T_A, which we calculate using standard 1D scattering matrix theory, depend exclusively on the transversal wave vector (i.e., Q_{ix} for T_E and Q_{fx} for T_A, before and after inelastic scattering by the molecule, respectively). In addition, we use the effective path length L', which is increased with respect to the width L of region II according to $L' = L/\cos\varphi_i$ (i.e., taking into account the oblique in-plane incidence angle of the electron φ_i relative to the gate normal). The wave vector after inelastic scattering is $Q_f = (Q_i^2 - Q_\omega^2)^{1/2}$, where $Q_\omega = \sqrt{2m^*\omega/\hbar}$, while the transversal component depends on scattering angle φ as $Q_{fx} = Q_f \cos(\varphi_i + \varphi)$. Putting these elements together and making the substitution $\Sigma_{\mathbf{Q}_i} \to (A/4\pi^2)\int d^2\mathbf{Q}_i$, we find $J = \int d\omega\, J(\omega)$, where

$$J(\omega) = \int_{Q_\omega}^{k_F} dQ_i\, J(\omega, Q_i) \tag{8}$$

with

$$J(\omega, Q_i) = \frac{-e\hbar L\, n_{\mathrm{mol}}}{2\pi^2 m^*} Q_i^2 \int_{-\pi/2}^{\pi/2} d\varphi_i\, T_E(Q_{ix}) \times \int_{-\pi/2-\varphi_i}^{\pi/2-\varphi_i} d\varphi\ \sigma_i^{\mathrm{mol}}(\omega,\varphi)\ T_A(Q_{fx}),$$

is the spectrally resolved inelastic current density, which is plotted in Fig. 3A, while J is shown in Fig. 3B. Here, $Q_{ix} = Q_i\cos\varphi_i$ and $k_F = (2m^*E_F)^{1/2}/\hbar$ is the Fermi wave vector in region I. Incidentally, we simplify the evaluation of the integral in Eq. 8 by realizing that the emitter gate produces a narrow transmission peak, which allows us to approximate $T_E(Q_{ix})$ by an energy δ–function (peaked at the quantum-well energy $E_i\cos^2\varphi_i = E^W$) times $(\pi/2)\Delta E^W$, where $\Delta E^W \approx 0.08$ meV at $E_i = 12$ meV (see Fig. 1). Incidentally, the dependence on incident electron energy $E_i = \hbar^2 Q_i^2/2m^*$ is readily given by $(m^*/\hbar^2 Q_i)J(\omega, Q_i)$, as shown in figs. S1 and S3.

Optical polarizability of 9-*cis* retinal

We model the orientation-averaged optical polarizability of this molecule as a scalar function formed by the sum of two Lorentzians, $\alpha(\omega) = \sum_{j=1,2} V_j\omega_j^2/[\omega_j^2 - \omega(\omega + i\gamma_j)]$, with parameters $V_1 = 0.3$ Å^3, $\hbar\omega_1 = 5.39$ meV, $\hbar\gamma_1 = 0.94$ meV, $V_2 = 0.7$ Å^3, $\hbar\omega_2 = 6.68$ meV, and $\hbar\gamma_2 = 0.77$ meV obtained by fitting measured IR absorption spectra (*47*). The optical absorption spectrum in Fig. 3B is obtained from $(4\pi\omega/c)$ Im $\{\alpha(\omega)\}$ (*60*).

SUPPLEMENTARY MATERIALS

Supplementary material for this article is available at http://advances.sciencemag.org/cgi/content/full/6/28/eabb4713/DC1

REFERENCES AND NOTES

1. J. N. Anker, W. P. Hall, O. Lyandres, N. C. Shah, J. Zhao, R. P. Van Duyne, Biosensing with plasmonic nanosensors. *Nat. Mater.* **7**, 442–453 (2008).
2. X. Qian, X.-H. Peng, D. O. Ansari, Q. Yin-Goen, G. Z. Chen, D. M. Shin, L. Yang, A. N. Young, M. D. Wang, S. Nie, In *vivo* tumor targeting and spectroscopic detection with surface-enhanced raman nanoparticle tags. *Nat. Biotech.* **26**, 83–90 (2008).
3. D. Lin, S. Feng, H. Huang, W. Chen, H. Shi, N. Liu, L. Chen, W. Chen, Y. Yu, R. Chen, Label-free detection of blood plasma using silver nanoparticle based surface-enhanced raman spectroscopy for esophageal cancer screening. *J. Biomed. Nanotech.* **10**, 478–484 (2014).
4. J. Ping, Z. Fan, M. Sindoro, Y. Ying, H. Zhang, Recent advances in sensing applications of two-dimensional transition metal dichalcogenide nanosheets and their composites. *Adv. Funct. Mater.* **27**, 1605817 (2017).
5. X. Yang, Z. Sun, T. Low, H. Hu, X. Guo, F. J. García de Abajo, P. Avouris, Q. Dai, Nanomaterial-based plasmon-enhanced infrared spectroscopy. *Adv. Mater.* **30**, 1704896 (2018).
6. J. Langer, D. J. de Aberasturi, J. Aizpurua, R. A. Alvarez-Puebla, B. Auguié, J. J. Baumberg, G. C. Bazan, S. E. J. Bell, A. Boisen, A. G. Brolo, J. Choo, D. Cialla-May, V. Deckert, L. Fabris, K. Faulds, F. J. García de Abajo, R. Goodacre, D. Graham, A. J. Haes, C. L. Haynes, C. Huck, T. Itoh, M. Käll, J. Kneipp, N. A. Kotov, H. Kuang, E. C. Le Ru, H. K. Lee, J.-F. Li, X. Y. Ling, S. A. Maier, T. Mayerhöfer, M. Moskovits, K. Murakoshi, J.-M. Nam, S. Nie, Y. Ozaki, I. Pastoriza-Santos, J. Perez-Juste, J. Popp, A. Pucci, S. Reich, B. Ren, G. C. Schatz, T. Shegai, S. Schlücker, L.-L. Tay, K. G. Thomas, Z.-Q. Tian, R. P. Van Duyne, T. Vo-Dinh, Y. Wang, K. A. Willets, C. Xu, H. Xu, Y. Xu, Y. S. Yamamoto, B. Zhao, L. M. Liz-Marzán, Present and future of surface-enhanced raman scattering. *ACS Nano* **14**, 28–117 (2020).
7. K. Kneipp, Y. Wang, H. Kneipp, L. T. Perelman, I. Itzkan, R. R. Dasari, M. S. Feld, Single molecule detection using surface-enhanced Raman scattering (SERS). *Phys. Rev. Lett.* **78**, 1667–1670 (1997).
8. S. Nie, S. R. Emory, Probing single molecules and single nanoparticles by surface-enhanced raman scattering. *Science* **275**, 1102–1106 (1997).
9. R. A. Álvarez-Puebla, L. M. Liz-Marzán, F. J. García de Abajo, Light concentration at the nanometer scale. *J. Phys. Chem. Lett.* **1**, 2428–2434 (2010).
10. M. Born, E. Wolf, *Principles of Optics: Electromagnetic Theory of Propagation, Interference and Diffraction of Light* (Cambridge University Press, Cambridge, 1999).
11. F. Huth, A. Govyadinov, S. Amarie, W. Nuansing, F. Keilmann, R. Hillenbrand, Nano-FTIR absorption spectroscopy of molecular fingerprints at 20 nm spatial resolution. *Nano Lett.* **12**, 3973–3978 (2012).
12. O. L. Krivanek, T. C. Lovejoy, N. Dellby, T. Aoki, R. W. Carpenter, P. Rez, E. Soignard, J. Zhu, P. E. Batson, M. J. Lagos, R. F. Egerton, P. A. Crozier, Vibrational spectroscopy in the electron microscope. *Nature* **514**, 209–214 (2014).
13. M. J. Lagos, A. Trügler, U. Hohenester, P. E. Batson, Mapping vibrational surface and bulk modes in a single nanocube. *Nature* **543**, 529–532 (2017).
14. R. Senga, K. Suenaga, P. Barone, S. Morishita, F. Mauri, T. Pichler, Position and momentum mapping of vibrations in graphene nanostructures in the electron microscope. *Nature* **573**, 247–250 (2019).

15. J. Nelayah, M. Kociak, O. Stéphan, F. J. García de Abajo, M. Tencé, L. Henrard, D. Taverna, I. Pastoriza-Santos, L. M. Liz-Marzán, C. Colliex, Mapping surface plasmons on a single metallic nanoparticle. *Nat. Phys.* **3**, 348–353 (2007).
16. M. Bosman, V. J. Keast, M. Watanabe, A. I. Maaroof, M. B. Cortie, Mapping surface plasmons at the nanometre scale with an electron beam. *Nanotechnology* **18**, 165505 (2007).
17. D. Rossouw, G. A. Botton, Plasmonic response of bent silver nanowires for nanophotonic subwavelength waveguiding. *Phys. Rev. Lett.* **110**, 066801 (2013).
18. G. Guzzinati, A. Béché, H. Lourenço-Martins, J. Martin, M. Kociak, J. Verbeeck, Probing the symmetry of the potential of localized surface plasmon resonances with phase-shaped electron beams. *Nat. Commun.* **8**, 14999 (2017).
19. P. Rez, T. Aoki, K. March, D. Gur, O. L. Krivanek, N. Dellby, T. C. Lovejoy, S. G. Wolf, H. Cohen, Damage-free vibrational spectroscopy of biological materials in the electron microscope. *Nat. Commun.* **7**, 10945 (2016).
20. J. A. Hachtel, J. Huang, I. Popovs, S. Jansone-Popova, J. K. Keum, J. Jakowski, T. C. Lovejoy, N. Dellby, O. L. Krivanek, J. C. Idrobo, Identification of site-specific isotopic labels by vibrational spectroscopy in the electron microscope. *Science* **363**, 525–528 (2019).
21. R. F. Egerton, Vibrational-loss eels and the avoidance of radiation damage. *Ultramicroscopy* **159**, 95–100 (2015).
22. S. F. Tan, L. Wu, J. K. W. Yang, P. Bai, M. Bosman, C. A. Nijhuis, Quantum plasmon resonances controlled by molecular tunnel junctions. *Science* **343**, 1496–1499 (2014).
23. F. J. García de Abajo, Optical excitations in electron microscopy. *Rev. Mod. Phys.* **82**, 209–275 (2010).
24. E. Bauer, Low-energy-electron microscopy. *Rep. Prog. Phys.* **57**, 895–938 (1994).
25. K. S. Novoselov, A. K. Geim, S. V. Morozov, D. Jiang, Y. Zhang, S. V. Dubonos, I. V. Grigorieva, A. A. Firsov, Electric field effect in atomically thin carbon films. *Science* **306**, 666–669 (2004).
26. A. H. Castro Neto, F. Guinea, N. M. R. Peres, K. S. Novoselov, A. K. Geim, The electronic properties of graphene. *Rev. Mod. Phys.* **81**, 109–162 (2009).
27. L. Wang, I. Meric, P. Y. Huang, Q. Gao, Y. Gao, H. Tran, T. Taniguchi, K. Watanabe, L. M. Campos, D. A. Muller, J. Guo, P. Kim, J. Hone, K. L. Shepard, C. R. Dean, One-dimensional electrical contact to a two-dimensional material. *Science* **342**, 614–617 (2013).
28. Q. H. Wang, K. Kalantar-Zadeh, A. Kis, J. N. Coleman, M. S. Strano, Electronics and optoelectronics of two-dimensional transition metal dichalcogenides. *Nat. Nanotech.* **7**, 699–712 (2012).
29. H. Zeng, G.-B. Liu, J. Dai, Y. Yan, B. Zhu, R. He, L. Xie, S. Xu, X. Chen, W. Yao, X. Cui, Optical signature of symmetry variations and spin-valley coupling in atomically thin tungsten dichalcogenides. *Sci. Rep.*, 1608 (2013).
30. K. F. Mak, C. Lee, J. Hone, J. Shan, T. F. Heinz, Atomically thin MoS_2: A new direct-gap semiconductor. *Phys. Rev. Lett.* **105**, 136805 (2010).
31. A. Splendiani, L. Sun, Y. Zhang, T. Li, J. Kim, C.-Y. Chim, G. Galli, F. Wang, Emerging photoluminescence in monolayer MoS_2. *Nano Lett.* **10**, 1271–1275 (2010).
32. C. Zhang, A. Johnson, C.-L. Hsu, L.-J. Li, C.-K. Shih, Direct imaging of band profile in single layer MoS_2 on graphite: Quasiparticle energy gap, metallic edge states, and edge band bending. *Nano Lett.* **14**, 2443–2447 (2014).
33. A. L. Elías, N. Perea-López, A. Castro-Beltrán, A. Berkdemir, R. Lv, S. Feng, A. D. Long, T. Hayashi, Y. A. Kim, M. Endo, H. R. Gutiérrez, N. R. Pradhan, L. Balicas, T. E. Mallouk, F. López-Urías, H. Terrones, M. Terrones, Controlled synthesis and transfer of large-area WS_2 sheets: From single layer to few layers. *ACS Nano* **7**, 5235–5242 (2013).
34. P. Johari, V. B. Shenoy, Tuning the electronic properties of semiconducting transition metal dichalcogenides by applying mechanical strains. *ACS Nano* **6**, 5449–5456 (2012).
35. D. M. Guzman, A. Strachan, Role of strain on electronic and mechanical response of semiconducting transition-metal dichalcogenide monolayers: An *ab-initio* study. *J. Appl. Phys.* **115**, 243701 (2014).
36. P. Lu, X. Wu, W. Guo, X. C. Zeng, Strain-dependent electronic and magnetic properties of MoS_2 monolayer, bilayer, nanoribbons and nanotubes. *Phys. Chem. Chem. Phys.* **14**, 13035–13040 (2012).
37. S. Chen, Z. Han, M. M. Elahi, K. M. M. Habib, L. Wang, B. Wen, Y. Gao, T. Taniguchi, K. Watanabe, J. Hone, A. W. Ghosh, C. R. Dean, Electron optics with p-n junctions in ballistic graphene. *Science* **353**, 1522–1525 (2016).
38. M.-H. Liu, C. Gorini, K. Richter, Creating and steering highly directional electron beams in graphene. *Phys. Rev. Lett.* **118**, 066801 (2017).
39. A. W. Barnard, A. Hughes, A. L. Sharpe, K. Watanabe, T. Taniguchi, D. Goldhaber-Gordon, Absorptive pinhole collimators for ballistic dirac fermions in graphene. *Nat. Commun.* **8**, 15418 (2017).
40. P. Bøggild, J. M. Caridad, C. Stampfer, G. Calogero, N. R. Papior, M. Brandbyge, A two-dimensional dirac fermion microscope. *Nat. Commun.* **8**, 15783 (2017).
41. M. D. Bachmann, A. L. Sharpe, A. W. Barnard, C. Putzke, M. König, S. Khim, D. Goldhaber-Gordon, A. P. Mackenzie, P. J. Moll, Super-geometric electron focusing on the hexagonal fermi surface of $PdCoO_2$. *Nat. Commun.* **10**, 5081 (2019).
42. F. Schedin, A. K. Geim, S. V. Morozov, E. W. Hill, P. Blake, M. I. Katsnelson, K. S. Novoselov, Detection of individual gas molecules adsorbed on graphene. *Nat. Mater.* **6**, 652–655 (2007).
43. E. Singh, M. Meyyappan, H. S. Nalwa, Flexible graphene-based wearable gas and chemical sensors. *ACS Appl. Mater. Interfaces* **9**, 34544–34586 (2017).
44. F. A. Rasmussen, K. S. Thygesen, Computational 2D materials database: Electronic structure of transition-metal dichalcogenides and oxides. *J. Phys. Chem. C* **119**, 13169–13183 (2015).
45. E. Burstein, S. Lundqvist, *Tunneling Phenomena in Solids* (Springer, 1969).
46. T. Sohier, M. Calandra, C.-H. Park, N. Bonini, N. Marzari, F. Mauri, Phonon-limited resistivity of graphene by first-principles calculations: Electron-phonon interactions, strain-induced gauge field, and boltzmann equation. *Phys. Rev. B* **90**, 125414 (2014).
47. M. Walther, B. Fischer, M. Schall, H. Helm, P. U. Jepsen, Far-infrared vibrational spectra of all-*trans*, 9-*cis* and 13-*cis* retinal measured by thz time-domain spectroscopy. *Chem. Phys. Lett.* **332**, 389–395 (2000).
48. L. L. Chang, L. Esaki, R. Tsu, Resonant tunneling in semiconductor double barriers. *Appl. Phys. Lett.* **24**, 593–595 (1974).
49. U. Sivan, M. Heiblum, C. P. Umbach, Hot ballistic transport and phonon emission in a two-dimensional electron gas. *Phys. Rev. Lett.* **63**, 992–995 (1989).
50. A. Palevski, M. Heiblum, C. P. Umbach, C. M. Knoedler, A. N. Broers, R. H. Koch, Lateral tunneling, ballistic transport, and spectroscopy in a two-dimensional electron gas. *Phys. Rev. Lett.* **62**, 1776–1779 (1989).
51. D. Alcaraz Iranzo, S. Nanot, E. J. C. Dias, I. Epstein, C. Peng, D. K. Efetov, M. B. Lundeberg, R. Parret, J. Osmond, J.-Y. Hong, J. Kong, D. R. Englund, N. M. R. Peres, F. H. L. Koppens, Probing the ultimate plasmon confinement limits with a van der waals heterostructure. *Science* **360**, 291–295 (2018).
52. S. de Vega, F. J. García de Abajo, Plasmon generation through electron tunneling in graphene. *ACS Photonics* **4**, 2367–2375 (2017).
53. W.-K. T, E. H. Hwang, S. D. Sarma, Ballistic hot electron transport in graphene. *Appl. Phys. Lett.* **93**, 023128 (2008).
54. J. Chen, V. Perebeinos, M. Freitag, J. Tsang, Q. Fu, J. Liu, P. Avouris, Bright infrared emission from electrically induced excitons in carbon nanotubes. *J. Laser Appl.* **310**, 1171–1174 (2005).
55. Z. M. Abd El-Fattah, V. Mkhitaryan, J. Brede, L. Fernández, C. Li, Q. Guo, A. Ghosh, A. Rodríguez Echarri, D. Naveh, F. Xia, J. E. Ortega, F. J. García de Abajo, Plasmonics in atomically thin crystalline silver films. *ACS Nano* **13**, 7771–7779 (2019).
56. C.-C. Shen, Y.-T. Hsu, L.-J. Li, H.-L. Liu, Charge dynamics and electronic structures of monolayer MoS_2 films grown by chemical vapor deposition. *Appl. Phys. Express* **6**, 125801 (2013).
57. W. Li, A. G. Birdwell, M. Amani, R. A. Burke, X. Ling, Y.-H. Lee, X. Liang, L. Peng, C. A. Richter, J. Kong, D. J. Gundlach, N. V. Nguyen, Broadband optical properties of large-area monolayer CVD molybdenum disulfide. *Phys. Rev. B* **90**, 195434 (2014).
58. E. J. C. Dias, F. J. García de Abajo, Fundamental limits to the coupling between light and 2D polaritons. *ACS Nano* **13**, 5184–5197 (2019).
59. S. Datta, *Electronic Transport in Mesoscopic Systems* (Cambridge University Press, Cambridge, 1995).
60. H. C. van de Hulst, *Light Scattering by Small Particles* (Dover, New York, 1981).

Acknowledgments

Funding: This work has been supported in part by the European Research Council (ERC Advanced Grant 789104-eNANO), the Spanish MINECO (MAT2017-88492-R and no. SEV2015-0522), the European Commission (Graphene Flagship 785219), the Catalan CERCA Program, the Fundació Privada Cellex, and the Fundació Mir-Puig. **Author contributions:** F.J.G.d.A. conceived the research, developed the theoretical formalism, and wrote the manuscript. R.Y. performed numerical simulations. Both authors discussed the results. **Competing interests:** The authors declare that they have no competing interests. **Data and materials availability:** All data needed to evaluate the conclusions in the paper are present in the paper and/or the Supplementary Materials. Additional data related to this paper may be requested from the authors.

Submitted 26 February 2020
Accepted 26 May 2020
Published 8 July 2020
10.1126/sciadv.abb4713

Citation: R. Yu, F. J. García de Abajo, Chemical identification through two-dimensional electron energy-loss spectroscopy. *Sci. Adv.* **6**, eabb4713 (2020).

Science Advances
AAAS

advances.sciencemag.org/cgi/content/full/6/28/eabb4713/DC1

Supplementary Materials for

Chemical identification through two-dimensional electron energy-loss spectroscopy

Renwen Yu and F. Javier García de Abajo*

*Corresponding author. Email: javier.garciadeabajo@nanophotonics.es

Published 8 July 2020, *Sci. Adv.* **6**, eabb4713 (2020)
DOI: 10.1126/sciadv.abb4713

This PDF file includes:

Figs. S1 to S4

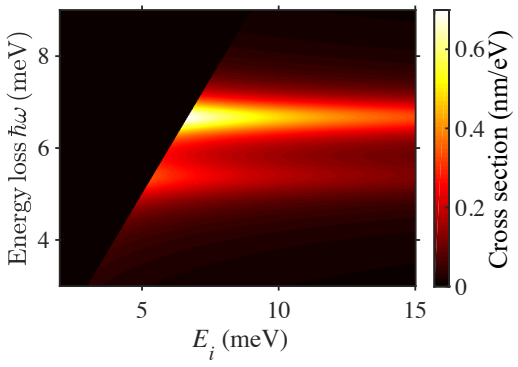

FIG. S1: Spectrally resolved inelastic electron-molecule cross section under the same conditions as in Fig. 1c, plotted here over a broad range of electron energies E_i for a molecule-surface separation distance $z_0 = 2\,\text{nm}$. A threshold energy $E_i = \hbar\omega$ is clearly visible in the data.

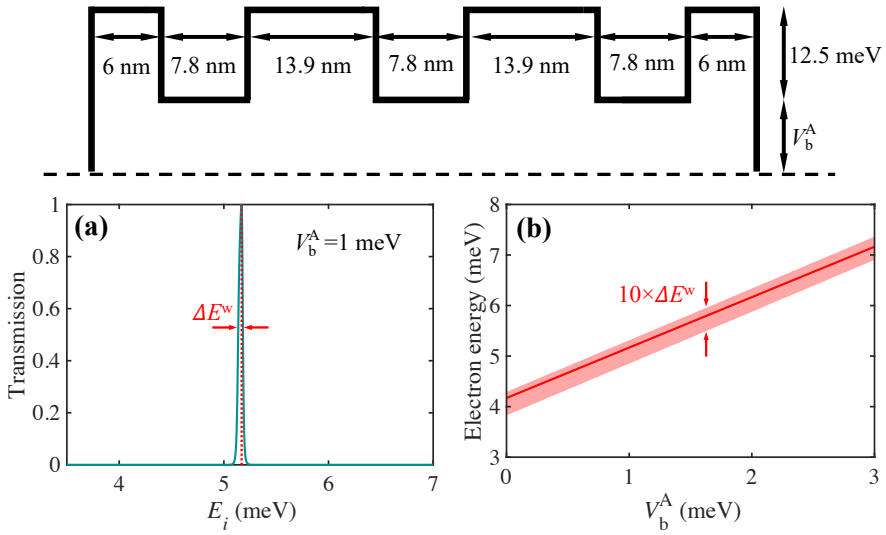

FIG. S2: Electron detection gate. **(a)** Transmission as a function of electron energy for the potential landscape shown in the upper inset with $V_b^A = 1\,\text{meV}$. **(b)** Peak transmission energy and FWHM as a function of bias voltage V_b^A. The potential landscape is designed such that no substantial additional transmission takes place for $E_i < 12.3\,\text{meV}$ in order to block elastic electrons injected at $E_i \sim 12\,\text{meV}$ from the emitter gate in the device considered in Fig. 3.

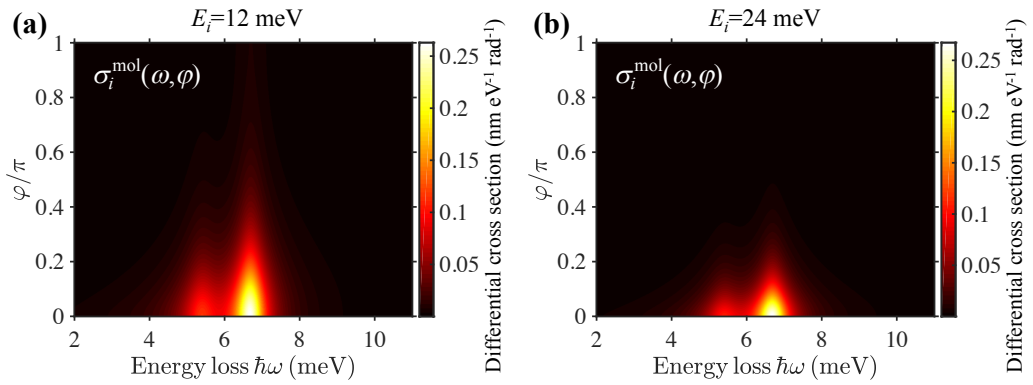

FIG. S3: Doubly differential cross section $\sigma_i^{\rm mol}(\omega,\varphi)$ under the same conditions as in Fig. 1c in (a) and for an incidence energy $E_i = 24\,\text{meV}$ in (b). The signal is strongly peaked along the forward direction, and effect that increases with E_i, while the signal strength scales roughly as $\sim 1/E_i$.

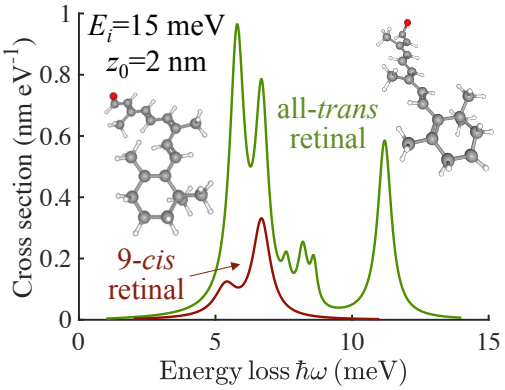

FIG. S4: Spectral cross section for the inelastic interaction between an electron plane wave of energy $E_i = 15\,\text{meV}$ moving in monolayer MoS_2 and a single molecule. We compare results for two different molecules (see labels) separated from the semiconductor by a distance $z_0 = 2\,\text{nm}$.